Experimental investigation of vortex-induced aeroelastic effects on a square cylinder in uniform flow

Dongmei Huang[1a], Teng Wu[*2] and Shiqing He[1b]

[1] *School of Civil Engineering, Central South University, Changsha, Hunan 410075, China*
[2] *Department of Civil, Structural and Environmental Engineering, University at Buffalo, Buffalo, NY 14260, USA*

Abstract. To investigate the motion-induced aeroelastic effects (or aerodynamic feedback effects) on a square cylinder in uniform flow, a series of wind tunnel tests involving the pressure measurement of a rigid model (RM) and simultaneous measurement of the pressure and vibration of an aeroelastic model (AM) have been systematically carried out. More specifically, the aerodynamic feedback effects on the structural responses, on the mean and root-mean-square wind pressures, on the power spectra and coherence functions of wind pressures at selected locations, and on the aerodynamic forces were investigated. The results indicated the vibration in the lock-in range made the shedding vortex more coherent and better organized, and hence presented unfavorable wind-induced effects on the structure. Whereas the vibration in the non-lock-in range generally showed insignificant effects on the flow structures surrounding the square cylinder.

Keywords: vortex-induced vibration; rigid model test; aeroelastic model test; square cylinder

1. Introduction

Vortex shedding typically occurs for bluff structures that are placed in fluids (e.g., Williamson 1996, Yen and Yang 2011). The vibrations of flexible structures at moderate wind speeds due to the vortex shedding are frequently observed (Ehsan and Scanlan 1990, Zasso *et al*. 2008, Belloli *et al*. 2011, 2014, Yen and Yang 2011, Wu and Kareem 2012, Ehrmann *et al*. 2014). The frequency of vortex shedding for each structure depends on a nondimensional Strouhal number relation (St = fD/U, where f is the dominate frequency component of the vortex-induced force; D is the front projection area of the structure cross-section per unit length; U is the oncoming flow velocity). As the frequency of shedding vortex-induced force is close to the natural frequency of the structure, the vortex-induced resonance occurs (Blevins 1990, Simiu and Scanlan 1996, Williamson and Govardhan 2008, Wu and Kareem 2013, Huang *et al*. 2014, Huang *et al*. 2017a, b). Due to the large amplitude of vortex-induced resonance, the structural vibrations present aerodynamic feedback effects (i.e., motion-induced aeroelastic effects) on vortex shedding. During this state, the Strouhal number relation breaks and the vortex shedding frequency is locked to the natural frequency of the structure (Sarpkaya 1979, Bearman 1984, Williamson and Govardhan 2008, Zasso *et al*. 2008, Chen and Xu 2012).

The vibration amplitude of structure and the wind speed range of the so-called lock-in phenomenon depend on a number of structural dynamics and aerodynamics parameters, such as the mass ratio, structural damping, Scruton number (*Sc*), Reynolds number, and body shape (Marra *et al*. 2011, Mannini *et al*. 2014).

There exist several experimental methods to clearly present the vortex shedding of a fixed or oscillating structure, such as the particle flow visualization with smoke lines (Yen and Hsu 2007) and particle image velocimetry (PIV) (Kikitsu *et al*. 2008, Yen and Yang 2011). However, these flow visualization approaches only show the vortex characteristics of wakes and cannot provide the detailed pressure-change characteristics of structural surfaces. Therefore, the vibration analysis of structures cannot be conducted directly, and an accurate theoretical analysis method cannot be accordingly established. To examine the vortex-induced forces on a rectangular high-rise building with a side ratio of two, the motion-induced across-wind forces acting on the structure were measured using a forced-vibration method by Katagiri *et al*. (2001). Mannini *et al*. (2014) investigated the vortex-induced forces and vibrations of a two-dimensional rectangular cylinder with a side ratio of 3:2 in the smooth flow based on both rigid and aeroelastic models. While the vortex-induced forces and responses of an oscillating two-dimensional or three-dimensional structure with a linear mode were investigated in the aforementioned studies, the aerodynamic feedback effects on dynamic responses, wind pressures, aerodynamic forces, and power spectra and coherence functions of wind loads based on a three-dimensional structure with more realistic nonlinear modes have not yet been systematically investigated in detail (e.g., Huang *et al*. 2015a). These more refined characteristics of the aerodynamic feedbacks may be critical to reveal the underlying physics of the vortex

---

*Corresponding author, Ph.D.
 E-mail: tengwu@buffalo.edu
[1a] Ph.D., E-mail: huangdongmei_tumu@163.com
[1b] Ph.D. Student, E-mail: 815472125@qq.com

(a) Mean wind speed profile

(b) Along-wind turbulence profile
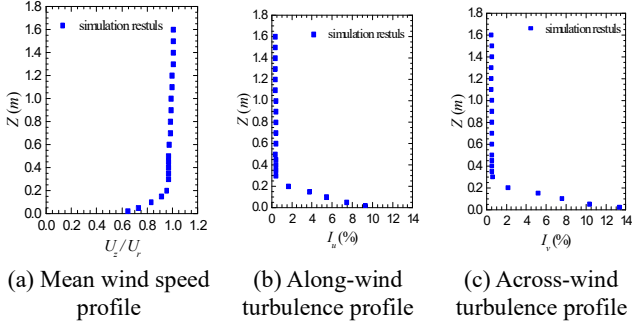
(c) Across-wind turbulence profile

Fig. 1 Simulation results of the flow field in the wind tunnel

induced forces and dynamic responses in non-lock-in and lock-in ranges, and will be the focus of the current study.

The rest of this study is organized as follows: Sect. 2 introduces the flow simulation and test model fabrication (based on a square cylinder) in the wind tunnel; Sect. 3 first presents the characteristics of wind-induced structural vibrations at various wind speeds, and then the aerodynamic feedback effects on the wind-induced response are discussed; Sect. 4 first investigates the aerodynamic feedback effects on the mean and root-mean-square (RMS) wind pressures, and the power spectra and coherence functions of wind pressures at selected locations, and then its effects on the aerodynamic forces at each measuring level and on the spectra of overall aerodynamic forces (in along-wind, across-wind and torsional directions) are examined; Sect. 5 discusses the relation between the vortex shedding and the displacement response in the vortex-induced resonance state; finally, the analysis results of the experimental tests based on the rigid model(RM) and aeroelastic model (AM) are summarized and presented.

2. Wind tunnel test setup

2.1 Flow field characteristics of wind tunnel

The experiments in this study were conducted in the wind tunnel system affiliated to the National Engineering Laboratory for High-Speed Railway Construction located at the Central South University of China. It is a close-circuit wind tunnel with two test sections. The low-speed test section with maximum wind speed of 20 m/s and turbulence intensity less than 1% is 12 m wide, 3.5 m high, and 18 m long, and the high-speed test section with maximum wind speed of 94 m/s and turbulence intensity less than 0.5% is 3 m wide, 3 m high, and 15 m long. All the tests in this study were conducted in the high-speed test section of the wind tunnel. The wind speeds at various heights were measured using Cobra probes, and that at height of 1.2 m is taken as the reference wind speed U_r. It was observed that the thickness of the ground boundary layer is approximately 0.3 m and the turbulence intensity beyond the boundary layer height is less than 0.5%. The simulated normalized mean wind speed (U_z/U_r), along-wind turbulence intensity (I_u) and cross-wind turbulence intensity (I_v) profiles are shown in Fig. 1.

2.2 Test models

To investigate the aerodynamic feedback effects on the surface pressures and wind-induced responses of a square cylinder, a RM and an AM are fabricated for wind tunnel tests. The RM of the square cylinder in the wind tunnel for pressure measurement in uniform air flow is shown in Fig. 2(a). The height of the model is 1.4 m and its width is 0.163 m, resulting in a block ratio of 2.5%. The wind speed at the reference height of 1.2 m is monitored by a pitot tube, and the wind pressure is measured in the experiments using the DSM3400 electronic scanning valve (manufactured by Scanivalve Corporation). The wind pressures have been measured at six different sections and there are 20 pressure taps at each section, as shown in Fig. 2(b). These 120 pressure taps are connected to the measurement system through PVC tubes for synchronous measurement. The sampling frequency is set at 625 Hz, and the sampling time is 32 s.

The AM of the square cylinder in the wind tunnel for pressure and vibration measurement in uniform air flow is shown in Figs. 3(a), and 3(b) shows the side view of the model. The skeleton of the AM consists of an I-beam steel mandrel and a few aluminum alloy supporting diaphragms, as shown in Fig. 3(c). Screws are drilled into the side edges of the diaphragms, which enables "coat" to be conveniently

(a) RM in the tunnel
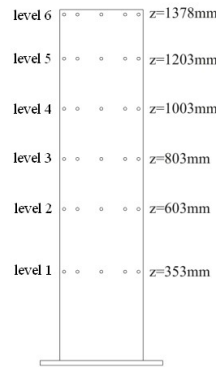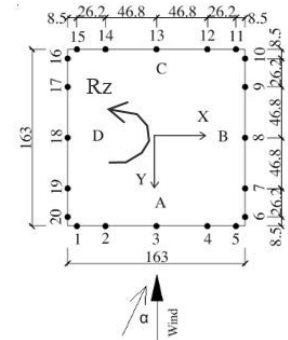
(b) Arrangement of pressure taps (unit: mm)

Fig. 2 Wind tunnel test setup for RM.

(a) AM in the tunnel   (b) Side view of AM   (c) Skeleton of AM   (d) Arrangement of pressure taps and laser displacement meters
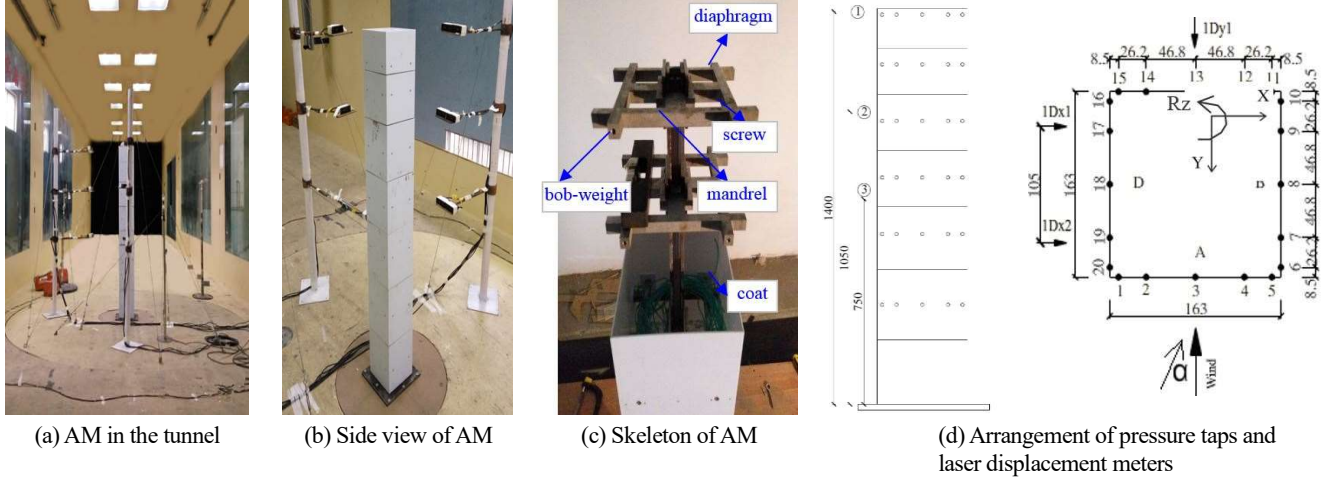
Fig. 3 Wind tunnel test setup for AM.

and securely connected with the diaphragms. The "coat" has been divided into seven sections fabricated by 2-mm-thick Plexiglas plates, as indicated in Figs. 3(b) and 3(c). The interval between two "coat" segments is approximately 2 mm to prevent possible collision during vibration. To correct the distortion of the dynamic pressure, signals are modified using the transfer function of tubing systems proposed by Holmes and Lewis (1987). In addition, the length of the pipeline is less than 200 mm with an internal diameter of 1.1mm. The bob-weight and scanning valve are placed on the diaphragm to adjust the mass and mass moment of inertia to modify the vibration modes of the model. The arrangement of pressure taps for the AM are same as that for the RM. The dynamic displacements of the AM are measured at three different sections with heights of 1400 mm, 1050 mm and 750 mm, and three laser displacement sensors (IL-300 made by Keyence) are placed at each section to measure the displacements in x direction at two locations and the displacement in y direction at one location, as shown in Fig. 3(d). The numbering of the measurement position consists of three parts, where the first part represents the number of the measuring level, the

second part indicates the direction of measurement, and the third part means the numbering of signals along a certain direction. For example, 1Dy1 indicates the first displacement signal along the y direction at measuring level No. 1, and 1Dx2 represents the second displacement signal along the x direction at measuring level No. 1. The sampling frequency for the displacements signals is set at 625 Hz, and the overall sampling data set size is 20, 478. Nine displacement measurement channels are recorded simultaneously. It should be noted that the vibration and wind pressure measurements are synchronized based on an in-house program, where the data acquisition systems of Scanning Valve (wind pressure measurement) and Laser Displacement Meter (vibration displacement measurement) can be simultaneously initiated (Huang and He 2016). In addition, the signals have been corrected to reduce the errors resulting from different delays of the two acquisition systems.

2.3 Modal parameters
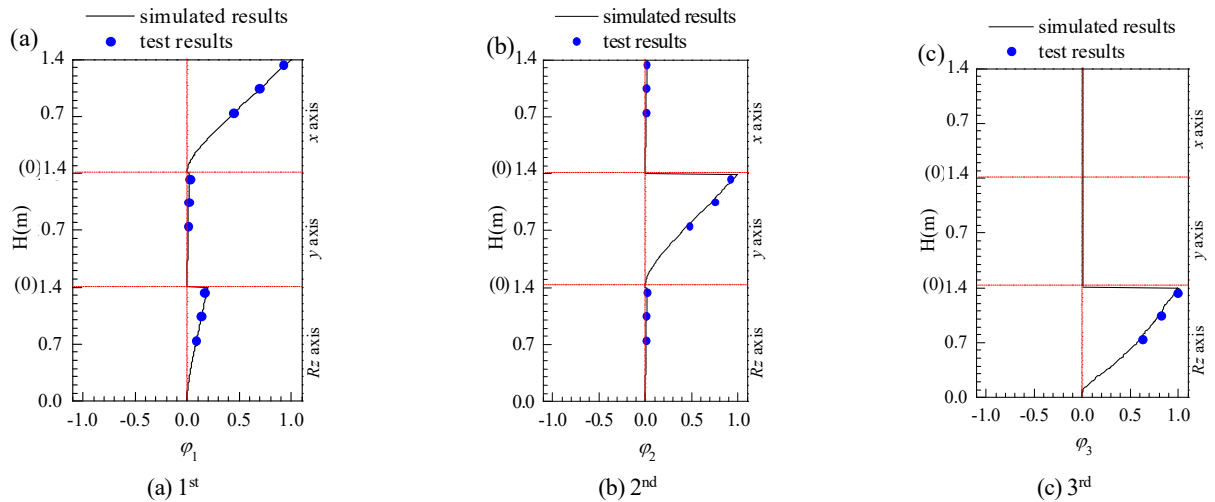
For the AM, the parameters of the first three vibration

(a) 1st   (b) 2nd   (c) 3rd

Fig. 4 Simulated and measured vibration modes: (a) 1st; (b) 2nd; (c) 3rd

Table 1 Modal parameters of AM

| Mode	Generalized mass M^*	Frequency (Hz)		Damping ratio ξ (%)	Scruton number
		simulation results	test results	test results	test results
1st (along x axis)	6.9088	5.5	5.54	0.38	4.9667
2nd (along y axis)	7.1805	6.5	6.44	0.41	5.5696
3st (around z axis)	0.0252	12.1	11.74	0.43	0.0205

modes obtained from the finite element analysis and the test results are presented in Table 1. The corresponding modal shapes on the centroids are shown in Fig. 4. The comparison of the results shows that the modal parameters identified from the tests are very close to those calculated using the finite element model. There are seven lumped points located on the corresponding diaphragms. Accordingly, totally 21 DOFs were considered. In the Table 1, the generalized mass is defined as (Dyrbye and Hansen 1996)

$$M^*_j = \frac{\boldsymbol{\varphi}_j^{\mathrm{T}} \mathbf{M} \boldsymbol{\varphi}_j}{\boldsymbol{\varphi}_j^{\mathrm{T}} \boldsymbol{\varphi}_j} \tag{1}$$
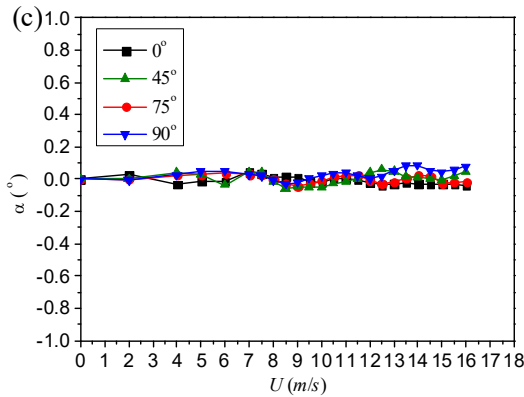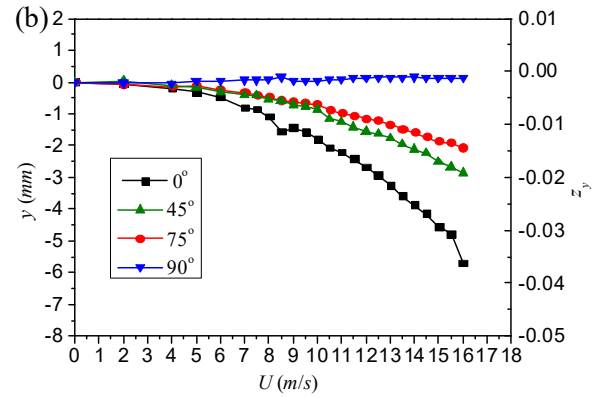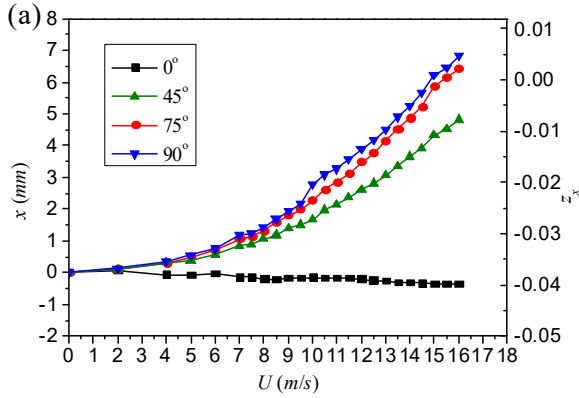
where the mass matrix $\mathbf{M}$ consists of mass and mass moment of inertia of each lumped point; $\boldsymbol{\varphi}_j$ is the jth mode shape.
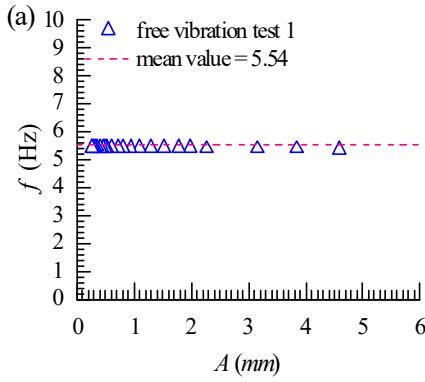
(a) Frequency vs. amplitude
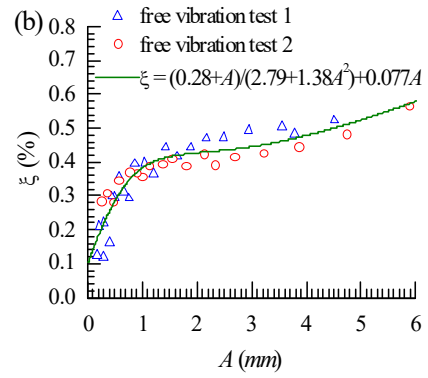
(b) Damping ratio vs. amplitude

Fig. 5 First (along x-axis) natural frequency and damping ratio of AM

Fig. 6 Mean displacement responses at top of model: (a) Along x axis; (b) Along y axis; (c) Around Rz axis

(a) Along *x* axis

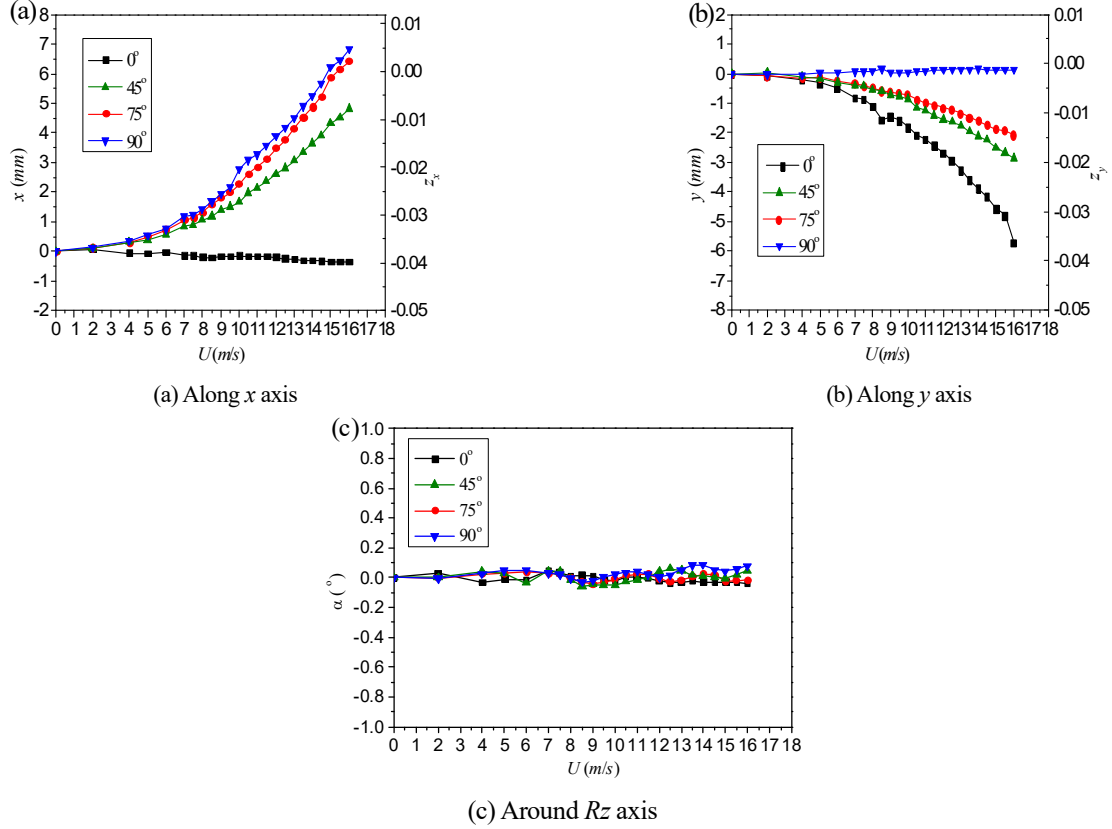
(b) Along *y* axis

(c) Around *Rz* axis

Fig. 7 RMS displacement responses at top of model

The Scruton number here is defined as (Dyrbye and Hansen 1996)

$$S_{C,j} = \frac{2\pi M_j^* \xi_j}{\rho D^2} \qquad (2)$$

where ρ is the air density; D is the cross-flow section dimension. The modal frequencies were identified using the peak method in frequency domain. The modal damping ratios were identified using the log decrement technique method and the results in Table 1 are the averaged values based on several vibration decay time histories.

Fig. 5 shows the identified 1st natural frequency (along the *x* axis) and the damping ratio of the AM with the amplitude. It can be observed that the natural frequency does not change with the amplitude, however, the damping ratio nonlinearly increases with the amplitude (Zasso *et al.* 2008). In this study, the relatively large damping ratios are selected to highlight the aerodynamic feedback effects on vortex-induced vibrations.

3. Aerodynamic feedback effects on wind-induced responses

3.1 Characteristics of wind-induced vibration

The vibration responses of the AM at various wind speeds are first analyzed. Figs. 6 and 7 show the mean and RMS displacement responses at the top of the model for different wind speeds and directions, respectively. The x and y axes at the wind angle of 90° refer to the along-wind

and across-wind directions, respectively. In the figures, the left ordinate axis indicates the actual mean or RMS displacement responses while the right ordinate axis implies the reduced mean or RMS values (i.e., $Z_x = X/D$, $Z_y = Y/D$, $\overline{\sigma} = \sigma_X/D$, and $\overline{\sigma}_y = \sigma_y/D$). As presented in Fig. 6, the along-wind response greatly decrease with the approaching wind angle and the torsional response for all the scenarios are small. Fig. 7 shows that the vortex-induced resonance occurs at a wind speed of 8.5 m/s for the wind attack angle of 0° and at a wind speed of 10 m/s for the wind attack angle of 90°. The responses in the across-wind and torsion directions increase significantly as vortex-induced resonance occurs, and the resonance amplitude of the 1st mode (at a wind speed of 8.5 m/s) in the across-wind and torsion directions with a relatively small damping ratio are larger than that of the 2nd mode (at a wind speed of 10 m/s). The significant resonance amplitude at the wind attack angle of 0° or 90° in the across-wind direction results in the occurrence of a flexural torsional coupling. Since no vortex-induced resonance is observed in the 45° and 75° wind directions, the scenario of 0° wind direction is focused in the following sections.

Fig. 8 presents the time histories of the across-wind displacement responses at the top of the test model in the 0° wind direction for two wind speeds, namely 8.5 m/s (when vortex-induced resonance occurs) and 10 m/s (when vortex-induced resonance does not occur). It is noted that the "beat" vibrations with significant amplitudes are observed when the model is subjected to the vortex-induced resonance, however, the vibration becomes random-like and
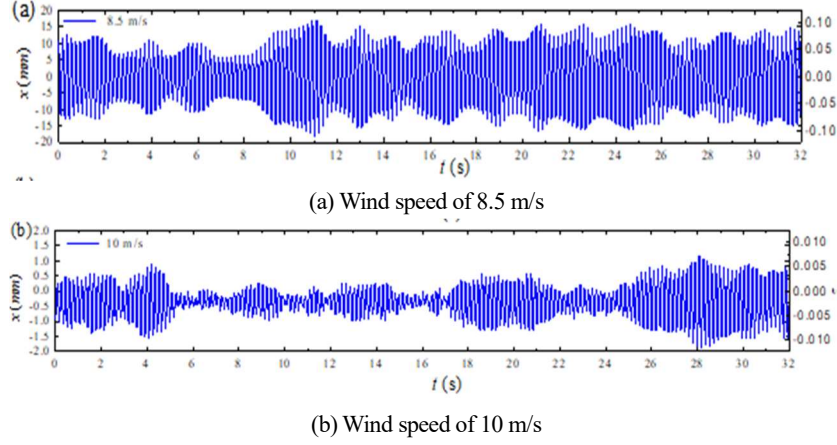
(a) Wind speed of 8.5 m/s

(b) Wind speed of 10 m/s

Fig. 8 Time histories of across-wind displacement responses at the top in the 0° wind direction

(a) Along *x* axis
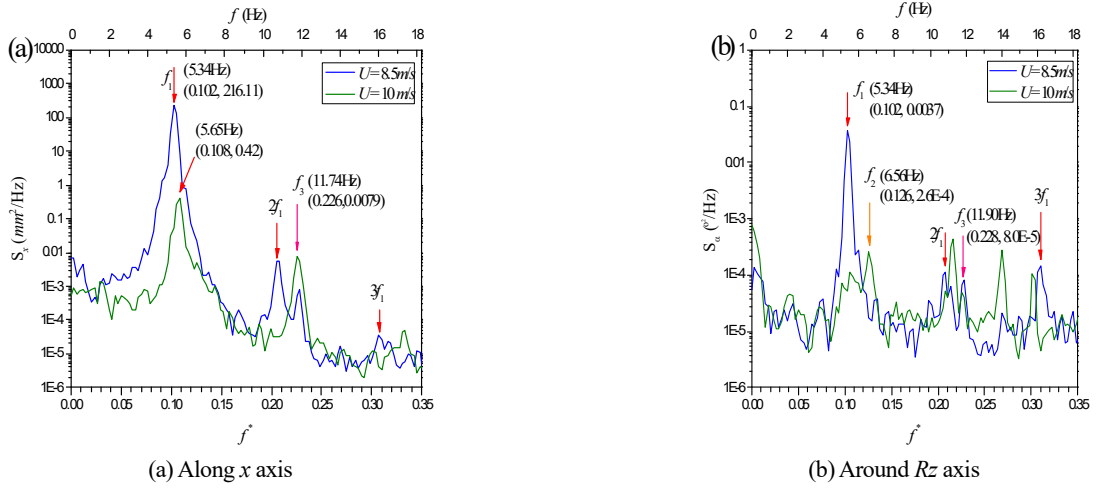

(b) Around *Rz* axis

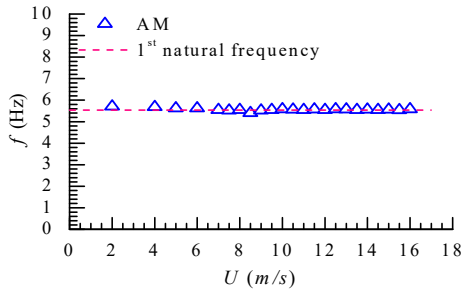Fig. 9 Power spectra of displacement responses at the top

Fig. 10 First (across-wind) vibration frequency of AM with wind speed

the amplitudes of the response decrease significantly when wind speed exceeds the lock-in region.

Fig. 9 shows the power spectra of the *x*- and *Rz*-axial displacement responses at the top of the test model for two wind speeds of 8.5 m/s and 10 m/s, where $f^*=f \cdot D/U_r$ is the reduced frequency and U_r is the mean wind speed at the reference point. When vortex-induced resonance occurs (U = 8.5 m/s), there is a significant peak close to the 1st (across-wind) frequency (5.34 Hz) in the across-wind direction. In addition, super harmonics are also observed in the response,

indicating nonlinear vibration characteristics. For the torsional response, a relatively larger peak also appears at the 1st natural frequency due to the existence of the bending torsion coupling effects, e.g., resulting from the mass eccentricity. The relatively smaller spectral peaks also appear in the vicinity of the natural frequency of torsional vibration (3rd mode). The spectral peak at the 1st natural frequency (across-wind vibration mode) decreases significantly as the wind speed is beyond the vortex-induced resonance range.

Fig. 10 gives the 1st (across-wind) vibration frequency of the AM with respect to the wind speed. It can be seen that the change of vibration frequency with wind speed is not apparent even at the wind speed of vortex-induced resonance. Hence, the aerodynamic feedback effects on the wind-induced vibration frequency are insignificant.

3.2 Aerodynamic feedback effects on wind-induced responses

To qualitatively and quantitatively examine the aerodynamic feedback effects on wind-induced responses for the square cylinder in uniform flow, three types of results are considered, namely the measured vibration results of AM, the calculated dynamic results of RM based on its pressure

measurements and the calculated dynamic results of AM based on its pressure measurements. More specifically, the wind-induced mean and RMS responses of the abovementioned scenarios were systematically investigated.

The averaged displacement at the height of z can be calculated as follows

$$\bar{y}_k(z) = \sum_{j=1}^{m} \varphi_j(z) \frac{\varphi_j^T \cdot \overline{F}}{\omega_j^2 M_j^*} \qquad (3)$$

where $\overline{F}$ is the averaged aerodynamic force vector on the test model, resulting from the wind pressure measurements at each measuring level; φ_j is the jth mode vector; ω_j is the jth structural

Fig. 11 Comparisons of mean along-wind displacement responses at the top

frequency; and M^*_j is the jth generalized mass. It is noted that the pressures on "coat" that are not measured in tests can be predicted using a BP-POD method (Huang *et al.* 2017c). Fig. 11 shows the mean along-wind responses at the top of the model for 0° wind direction under four situations. In the figure, the calculated results of RM are based on a lumped mass model (Huang *et al.* 2015b), where the masses and mass moment of inertias are condensed at the centralities of the diaphragms. The calculated results of AM-1 and AM-2 are based on a lumped mass model and a high-fidelity finite element model, respectively. As presented in the figure, the aerodynamic feedback effects on the wind-induced mean responses of the square cylinder in uniform flow are generally insignificant. The "favorable" effects occur for small mean responses or wind speeds. The "unfavorable" effects for mean responses (i.e., response increase due to the aerodynamic feedback effects) are mainly at the wind speed of vortex-induced resonance (8.5 m/s) and the wind speeds larger than 12 m/s. In general, the difference between the four conditions remains below 20%. Compared to the AM-1 results, the calculated mean responses of AM-2 are slightly closer to the measured results in the wind tunnel.

Fig. 12 presents the RMS wind-induced responses at the top of the model for the abovementioned four scenarios, where the extended method of covariance proper transformation-based pseudo excitation algorithm (POD-PEA) (Huang *et al.* 2015) in the frequency domain was used for the calculation of RM and AM-1 cases and the Runge–Kutta method in the time-domain was employed for the calculation of AM-2 case. As shown in the figure, the aerodynamic feedback effects on the
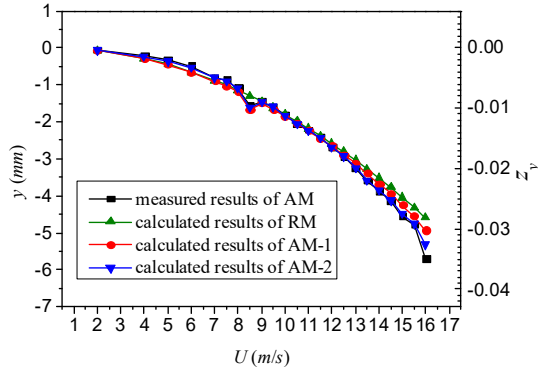

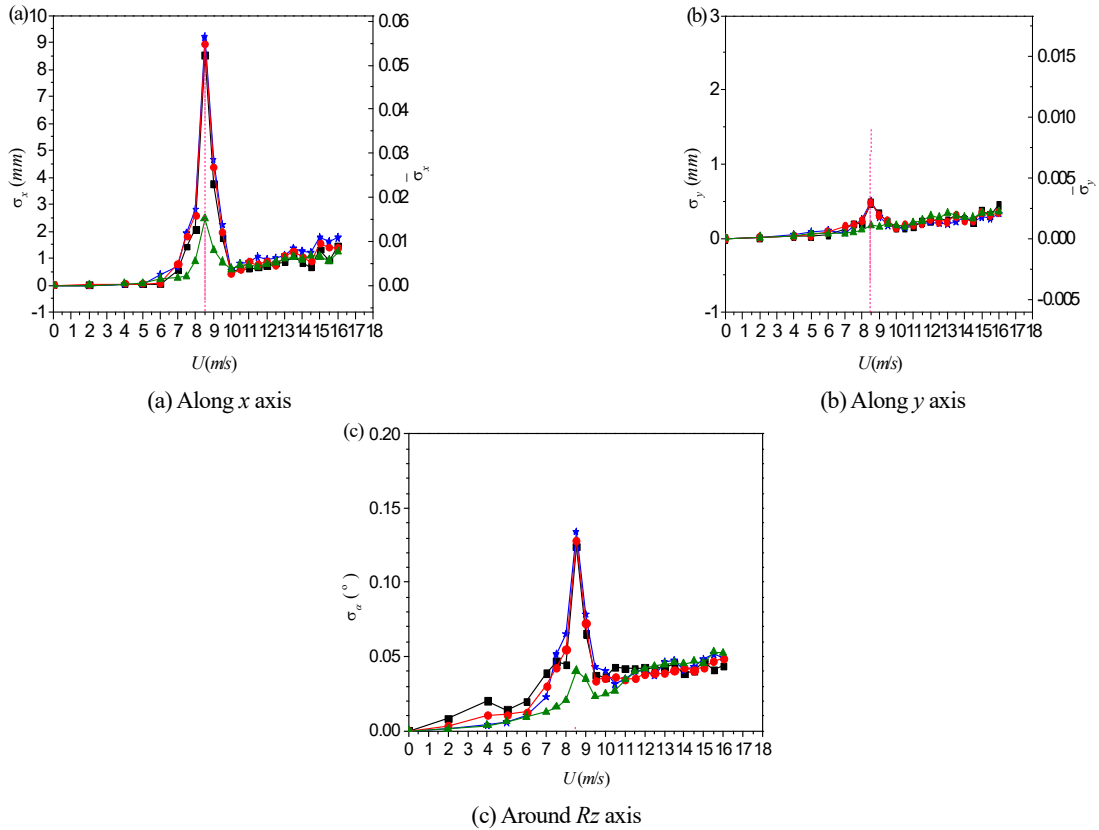(a) Along *x* axis

(b) Along *y* axis

(c) Around *Rz* axis

Fig. 12 Comparison of RMS displacement responses at the top

wind-induced dynamic responses of the square cylinder in a uniform flow are remarkable in the lock-in region, indicating the large motion enhances the regularity and energy of vortex shedding. The dynamic responses without consideration of the aerodynamic feedback effects (i.e., the calculated results of RM) are approximately a quarter of those involving aerodynamic feedback contributions (i.e., the calculated results of AM or measured results). In the non-lock-in region, the aerodynamic feedback effects on the wind-induced dynamic responses are insignificant. Compared to the AM-1 results, the calculated dynamic responses of AM-2 are slightly closer to the measured results in the wind tunnel.

4. Aerodynamic feedback effects on wind pressures and aerodynamic forces

The aerodynamic feedback effects are typically characterized by the linear or nonlinear aerodynamic damping in the analysis of structural dynamics (e.g., Ehsan and Scanlan1990, Gu and Quan 2004, Marra *et al.* 2011, Zhu *et al.* 2013, Wu and Kareem 2015, Huang *et al.* 2018, Zheng *et al.* 2019). To further investigate the underlying mechanics of the aerodynamic feedback contributions to the dynamic response, the aerodynamic feedback effects on the wind-induced pressures and forces on AM are measured in the wind tunnel tests together with structural vibrations.

4.1 Aerodynamic feedback effects on wind pressures

Figs. 13 and 14 show the mean and RMS wind pressure coefficients of the AM at various measuring levels for the wind speeds of 6 m/s (before vortex-induced resonance), 8.5 m/s (during vortex-induced resonance) and 10 m/s (after vortex-induced resonance). As shown in Fig. 13, there is a slight change for the mean wind pressure coefficients before and after the vortex-induced resonance. On the other hand, compared to the non-lock-in range, the absolute values of the pressures in the negative pressure zone increase obviously when vortex-induced resonance occurs (within 1.5 times). This observation illustrates that the enhanced vortex shedding effect in lock-in region would enlarge the mean values of the suction on a square cylinder in uniform air flow. As shown in Fig. 14, the RMS wind pressure coefficients change noticeably in the different vibration states. Compared to the non-lock-in region, the fluctuating wind pressure coefficients in the negative pressure area (lateral sides and leeward side) increase significantly when vortex-induced resonance occurs. The fluctuating wind pressure coefficients at $U = 6$ m/s are larger than those at $U = 10$ m/s. The results demonstrate that the aerodynamic feedback effects on the RMS wind pressure coefficients of a square cylinder is significant at lock-in region.

To highlight the aeroelastic effects on the surface wind pressures, the measuring levels 4 and 6 are considered in detail. More specifically, the mean and RMS results of AM at the
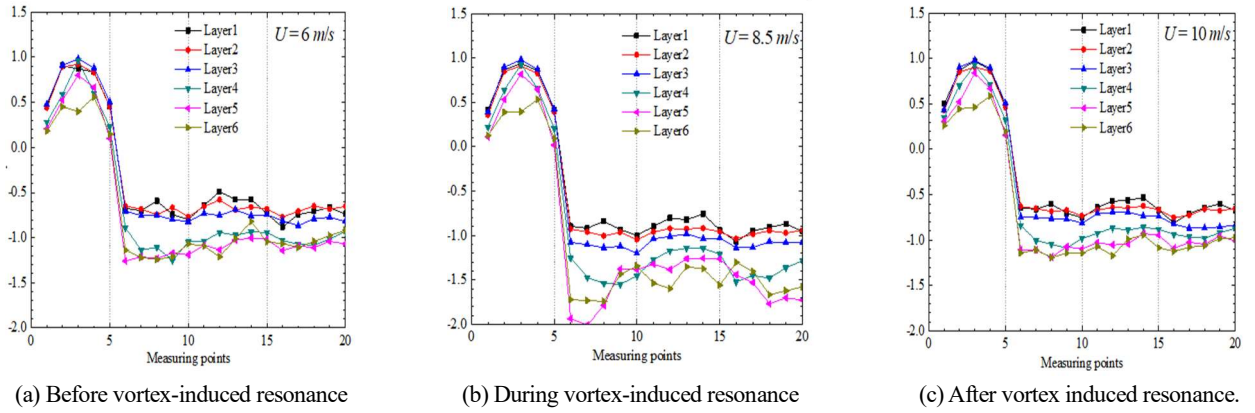

| (a) Before vortex-induced resonance | (b) During vortex-induced resonance | (c) After vortex induced resonance. |

Fig. 13 Mean wind pressure coefficients of AM at each measuring level

| (a) Before vortex-induced resonance | (b) During vortex-induced resonance | (c) After vortex induced resonance |
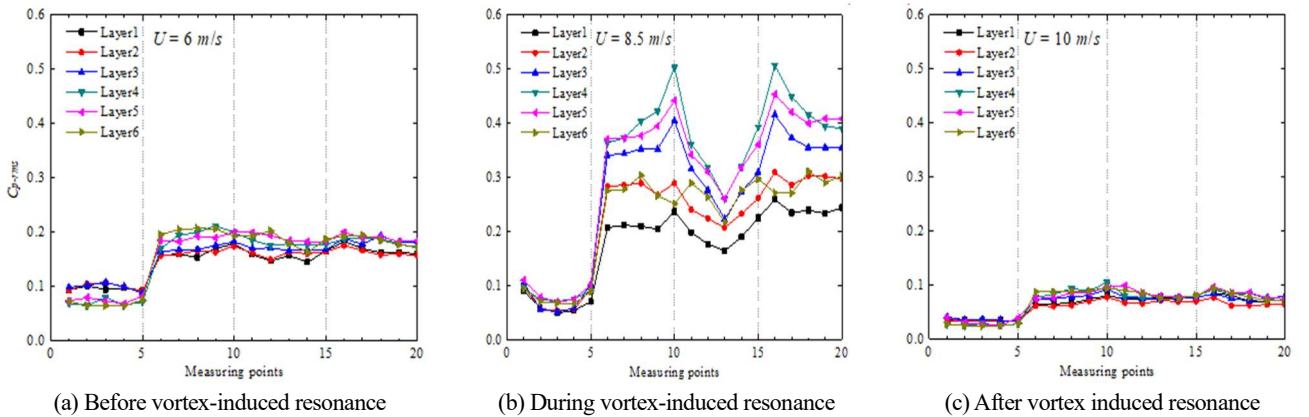
Fig. 14 RMS wind pressure coefficients on of the AM for each measuring level

(a) Middle level - 4th   (b) Top level - 6th
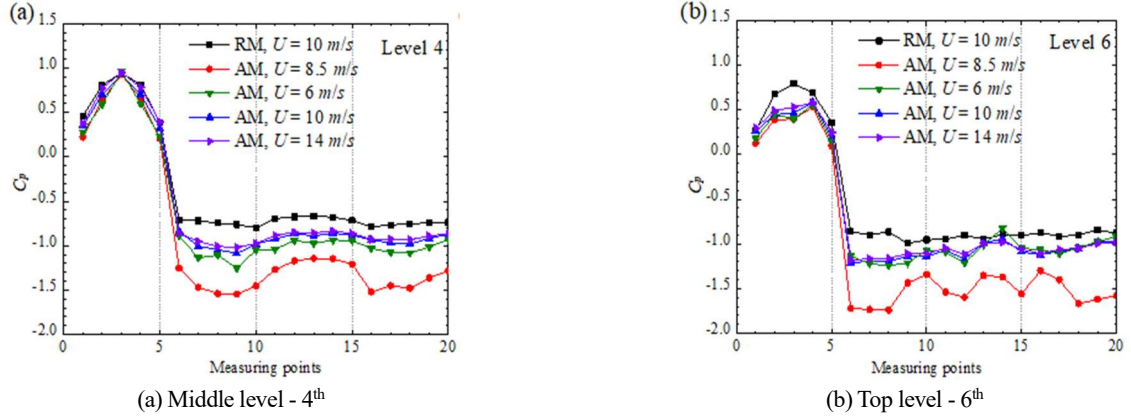
Fig. 15 Comparisons of mean wind pressure coefficients in different vibration states

(a) Middle level - 4th   (b) Top level - 6th
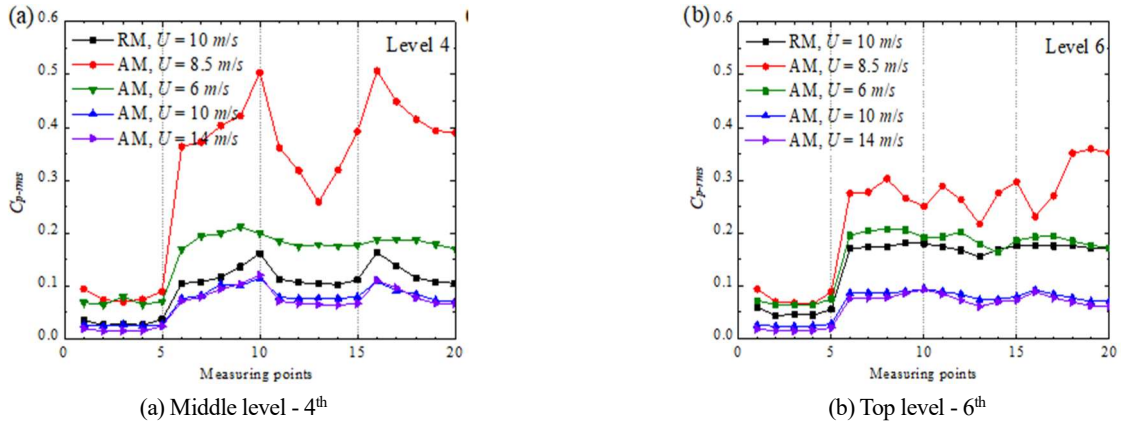
Fig. 16 Comparisons of RMS wind pressure coefficients in different vibration states

(a) RM with $f^* = 0.104$ at wind speed of 14 m/s   (b) AM with $f^* = 0.103$ at wind speed of 8.5 m/s
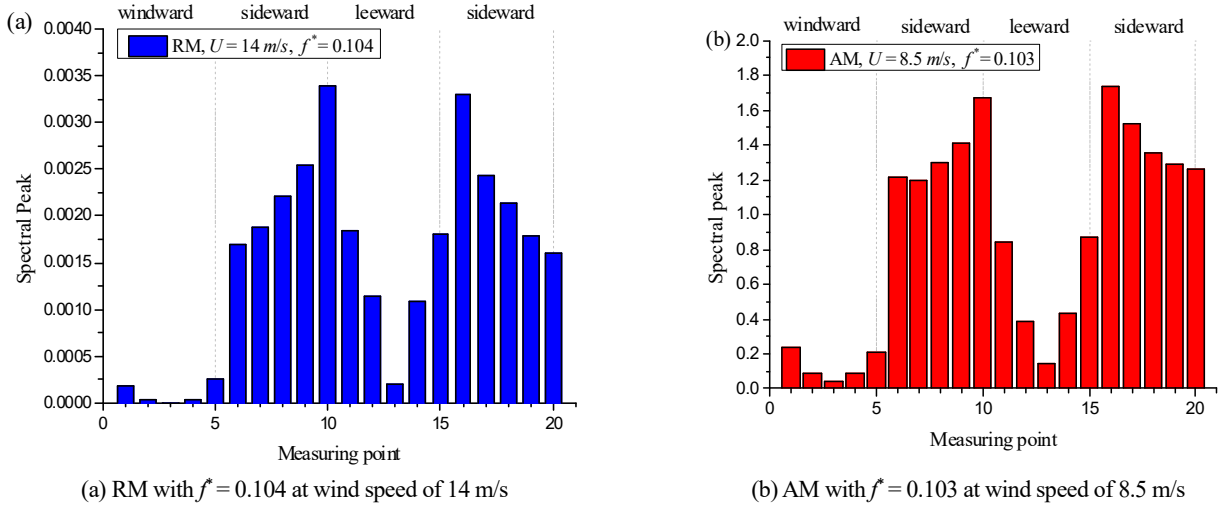
Fig. 17 Distributions of the spectral peaks of pressure coefficients on measuring level 4 of RM and AM

wind speeds of 6 m/s, 8.5 m/s, 10 m/s and 14 m/s are compared with those of RM at $U = 10$ m/s, as shown in Figs. 15 and 16. When the AM creates vortex-induced resonance ($U = 8.5$ m/s), the absolute mean pressure coefficients in the negative pressure area (lateral sides and leeward side) are significantly higher than those of the RM with stationary state. However, the coefficients on the positive pressure area

decrease slightly. Furthermore, the RMS wind pressure coefficients of the AM are significantly higher than those of the RM, especially for the lateral and leeward sides at the middle level. When the AM exhibits stochastic vibration, the absolute mean wind pressure coefficients in the negative pressure zone increase slightly in comparison with those of the RM, while the coefficients in the positive pressure zone decrease slightly. In
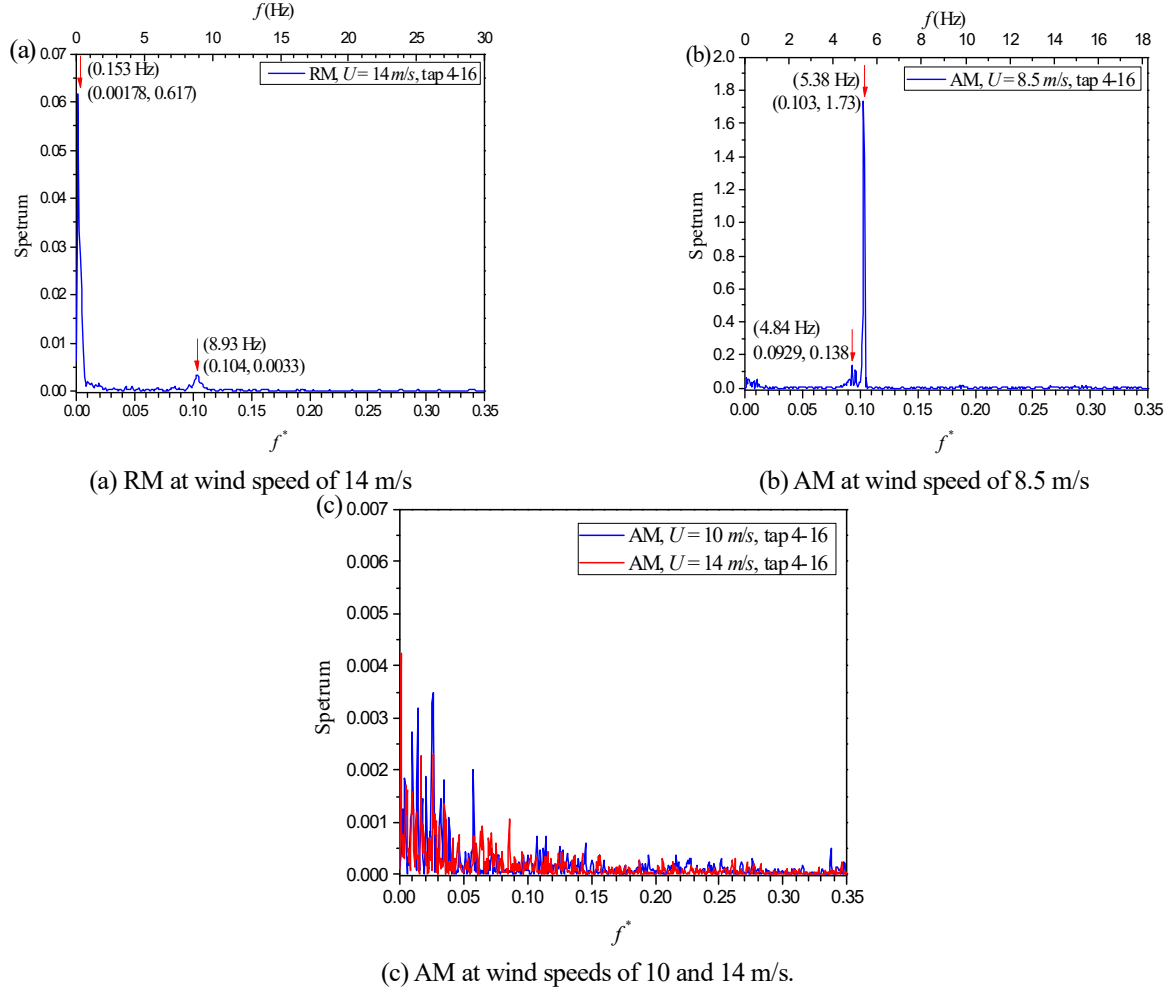
(a) RM at wind speed of 14 m/s

(b) AM at wind speed of 8.5 m/s

(c) AM at wind speeds of 10 and 14 m/s.

Fig. 18 Power spectra of the pressure coefficients for tap 4-16

(a) Dominant frequency vs. wind speed
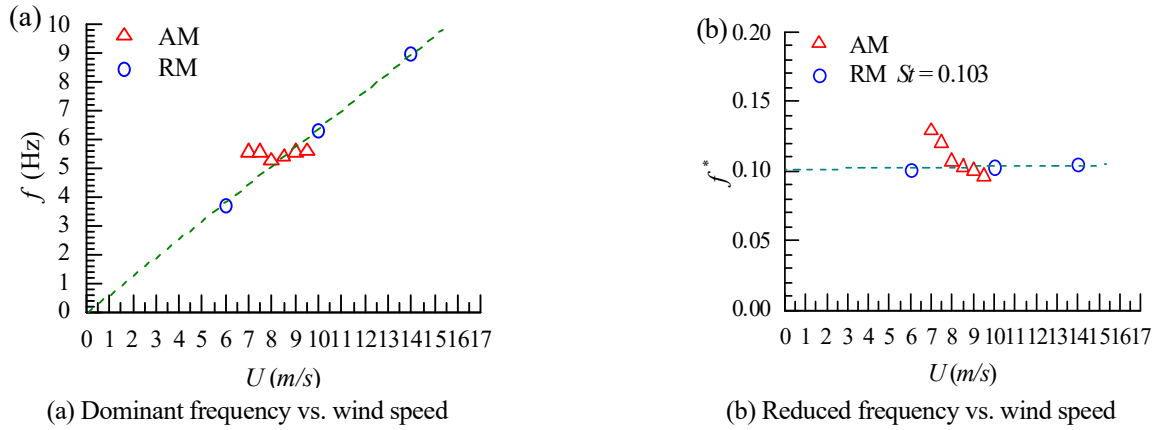
(b) Reduced frequency vs. wind speed

Fig. 19 Changes of dominant frequency and reduced frequency of pressure coefficients for tap 4-16

addition, the RMS wind pressure coefficients on all the faces of the AM increase compared to those of the RM at the same wind speed. It is noted that the influence of wind speeds on the mean wind pressure is insignificant. On the other hand, the RMS values tend to decrease with the wind speed up to $U = 10$ m/s.

To examine the distributions of vortex shedding energy around the square cylinder in a uniform flow for RM and AM

at different vibration states, Fig. 17 presents the distributions of the spectral peaks of the pressure coefficients on measuring level 4 of both AM and RM models at selected wind speeds. It is shown that the position of the maximum energy of vortex shedding is at the rear edge of the lateral side. Near the reduced frequency of approximately $f^* = 0.103$ (corresponding to St relation of square section with the 1st natural frequency of AM), the spectral peaks of the AM at the wind speed of 8.5

m/s (in lock-in state) are far greater than those of the RM (in stationary state at $U = 14$ m/s).

The tap 16 located at the rear edge of the lateral side at measuring level 4 (tap 4-16) was considered to present the detailed characteristics of power spectrum of the pressure coefficient, as shown in Fig. 18. In the figure, the lower abscissa axis expresses the reduced frequency, and the upper abscissa axis represents the actual frequency. Fig. 18(a) shows that the power spectrum of the RM has two obvious peaks, one occurring at the very low frequency (0.153 Hz) and the other at a frequency of 8.93 Hz (reduced frequency $f^* = 0.104$). The peak at low frequency is mainly produced by a large-scale low-frequency wake vortex of the model in the uniform flow field, and the peak at 8.93 Hz is mainly related to the vortex related to structural characteristic size. Although the energy of the peak at low frequency is large, it is difficult to induce the significant model vibration because of its low frequency (much lower than the natural frequency of the model, as shown in Table 1).

However, the peak at 8.93 Hz may be subjected to vortex-induced resonances at certain wind speeds. As shown in Fig. 18(b), when the AM produces vortex-induced resonance at

$U = 8.5$ m/s, in addition to the vortex shedding peak at 4.84 Hz (reduced frequency of 0.0929, a little smaller than St) a more pronounced peak is observed at 5.38 Hz (reduced frequency of 0.103), very close to the 1st natural frequency of the structure (5.54 Hz, as show in Table 1). The intensive and regular vibrations of the structure result in remarkable effects on the vortex shedding, and hence generating large self-excited forces close to the natural frequency of the structure. Fig. 18(c) shows the power spectra of wind pressure coefficients of tap 4-16 at 10 m/s and 14 m/s wind speeds. The figure also shows that no spectral peak exists near the St relation ($f^* = 0.104$). The results in Figs. 18(a)-(c) shows that the vortex shedding associated with the size feature of the structure is observed to have large energy in the vortex-excited resonance ($U = 8.5$ m/s) of the AM, compared to that of the RM. However, the energy of vortex shedding for the AM with stochastic vibrations at certain wind speed is smaller than that of the stationary RM.

Fig. 19 shows the changes in dominant frequency and reduced frequency of pressure coefficients for tap 4-16. It can be observed that the vortex shedding frequency increases linearly with the wind speed for the RM with stationary state. However, the vortex shedding only occurs in the lock-in wind

(a) Taps 4-16 & 5-16

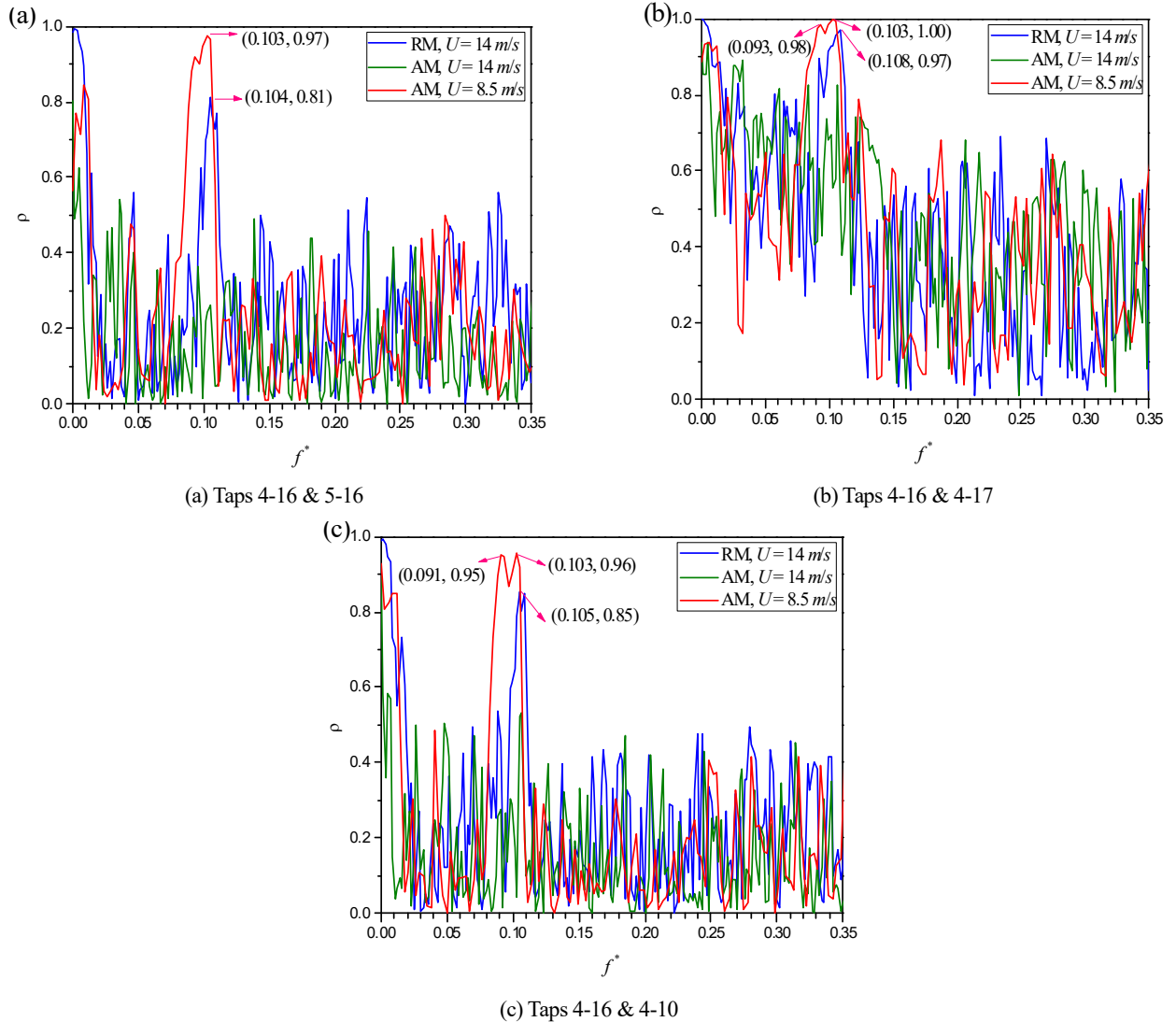(b) Taps 4-16 & 4-17

(c) Taps 4-16 & 4-10

Fig. 20 Coherence functions of the pressure coefficients

speed range when the model is in the vibration state, and its frequency basically remains unchanged in lock-in range. Correspondingly, the reduced frequency basically linearly decreases with the wind speed.

Fig. 20 provides the coherence functions of the pressure coefficients of selected taps on AM and RM at several wind speeds. For the RM at $U = 14$ m/s and AM subjected to vortex-induced resonance ($U = 8.5$ m/s), the coherence functions of taps 4-16 and 5-16 (top and bottom measuring points on the same side), taps 4-16 and 4-17 (front and rear measuring points on the same side), and taps 4-16 and 4-10 (the corresponding measuring points on two sides) show significant peaks near St relation of the square cylinder (i.e., the reduced frequency is approximately 0.103). However, the coherence functions near St relation have no obvious peaks when the AM only displays stochastic vibrations at $U = 14$ m/s, indicating that the regularity of vortex shedding at this time is weakened and

destroyed because of irregular random vibration of the structure. At relatively low frequencies, the coherence function values of the three abovementioned sets of measuring points in three states from high to low are as follows: RM ($U = 14$ m/s), AM in vortex-excited resonance state ($U = 8.5$ m/s), and AM subject to random buffeting ($U = 14$ m/s). Near the St relation (i.e., the reduced frequency is approximately 0.103), however, the coherence function values of the three sets of measuring points in three states from high to low are as follows: AM in vortex-excited resonance state ($U = 8.5$ m/s), RM ($U = 14$ m/s), and AM subject to random buffeting ($U = 14$ m/s). The comparisons show that the vibration will have a certain disturbance to the large eddy at the low frequency, considerably different from the natural frequency of the structure, and the disturbance by irregular vibration shows even more obvious effects. The regular vortex-induced resonance has a strengthening effect on the characteristic

(a) Taps 4-16 & 5-16

(b) Taps 4-16 & 4-17
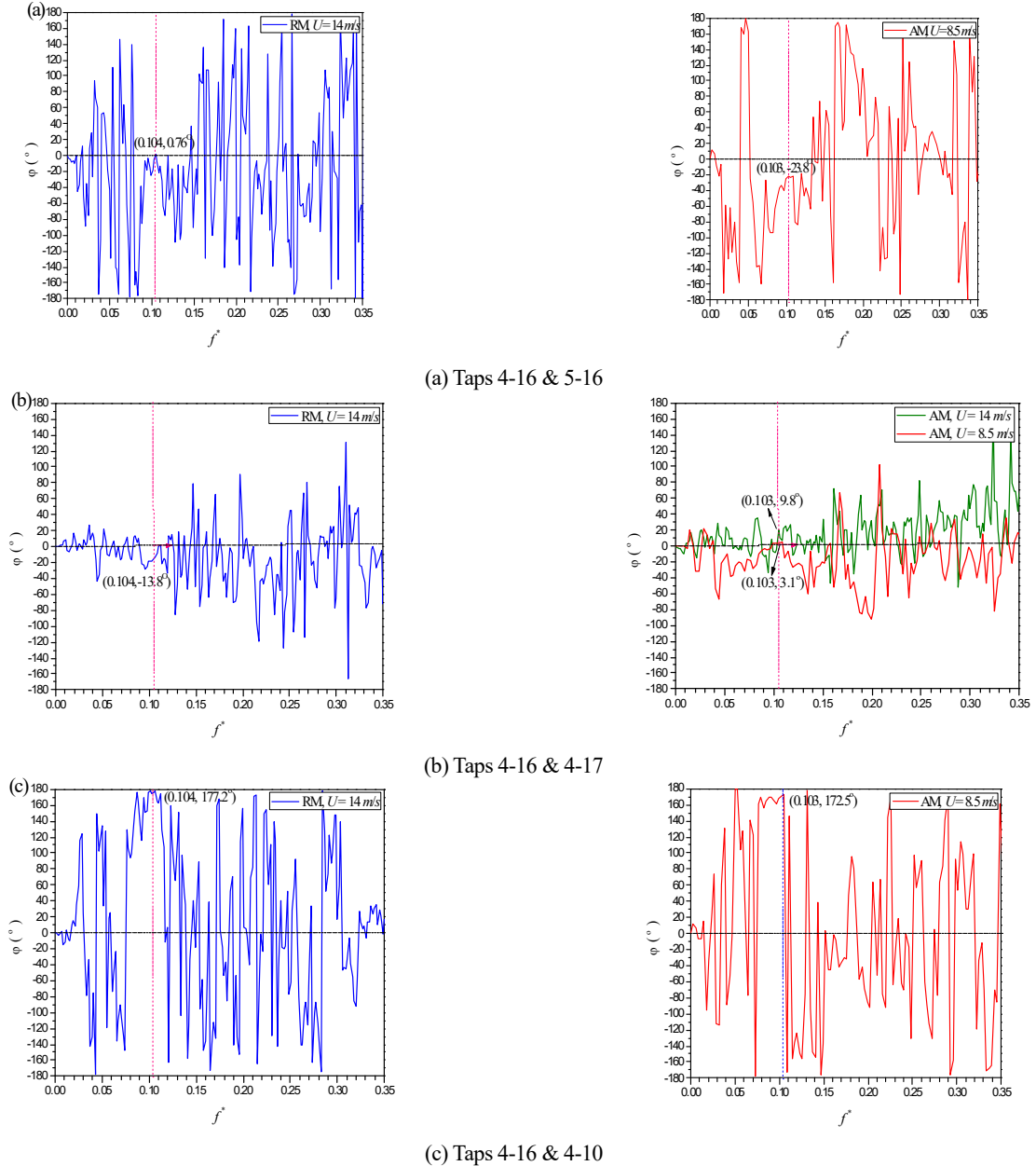

(c) Taps 4-16 & 4-10

Fig. 21 Phase angles of the pressure coefficients

vortices near the natural frequencies of structures, while the irregular random vibration would suppress the characteristic vortices. The reduced frequency of the vortex shedding of the AM in vortex-induced resonance state ($U = 8.5$ m/s) is slightly smaller than that of the RM ($U = 14$ m/s) due partially to the aerodynamic stiffness effects, and the frequency range is slightly wider for the lock-in feature. In addition, the correlation between the wind pressures of the measuring points decrease with their distance.
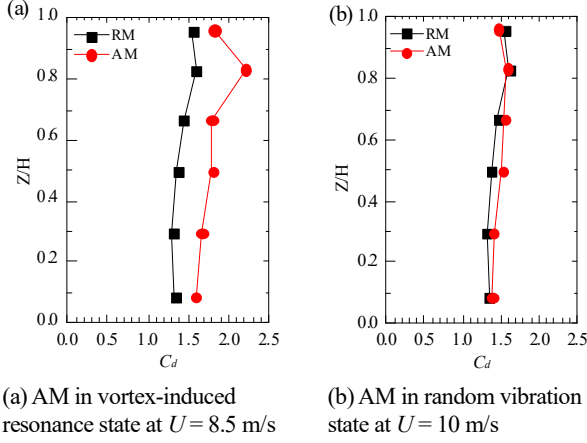
To analyze the temporal and spatial features of vortex shedding at different measuring points, Fig. 21 shows the phase angles of the pressure coefficients of selected taps on AM and RM at several wind speeds. For the RM at $U = 14$ m/s and the AM subjected to vortex-induced resonance ($U = 8.5$ m/s), the phase angles of taps 4-16 & 5-16 (upper and lower measuring points on the same side) and taps 4-16 & 4-17 (front and rear measuring points on the same side) near St relation (i.e., the reduced frequency is approximately 0.103) of the square cylinder are very small, indicating a very large vortex shedding on the same side. On the other hand, the phase angle of the AM has a certain lag of $-23.8°$ due possibly to the existence of the bending and torsional coupling effects. For the RM at $U = 14$ m/s and the AM subjected to vortex-induced resonance ($U = 8.5$ m/s), the phase angles of taps 4-16 & 4-10 (corresponding measuring points to two lateral sides) near the St relation of a square cylinder are close to 180°, which illustrates that the vortex shedding alternately acts on two lateral sides. When the AM is subject to stochastic vibration ($U = 14$ m/s), the phase angle of taps 4-16 & 4-17 (front and rear measuring points on the same side) near St relation is very small, while the phase angles of taps 4-16 & 5-16 (the upper and lower measuring points on the same side) and taps 4-16 & 4-10 (corresponding measuring points on two lateral sides) present random-like features. This observation indicates that the characteristic vortex in this state is regular at a relatively small scale (between taps 4-16 & 4-17).
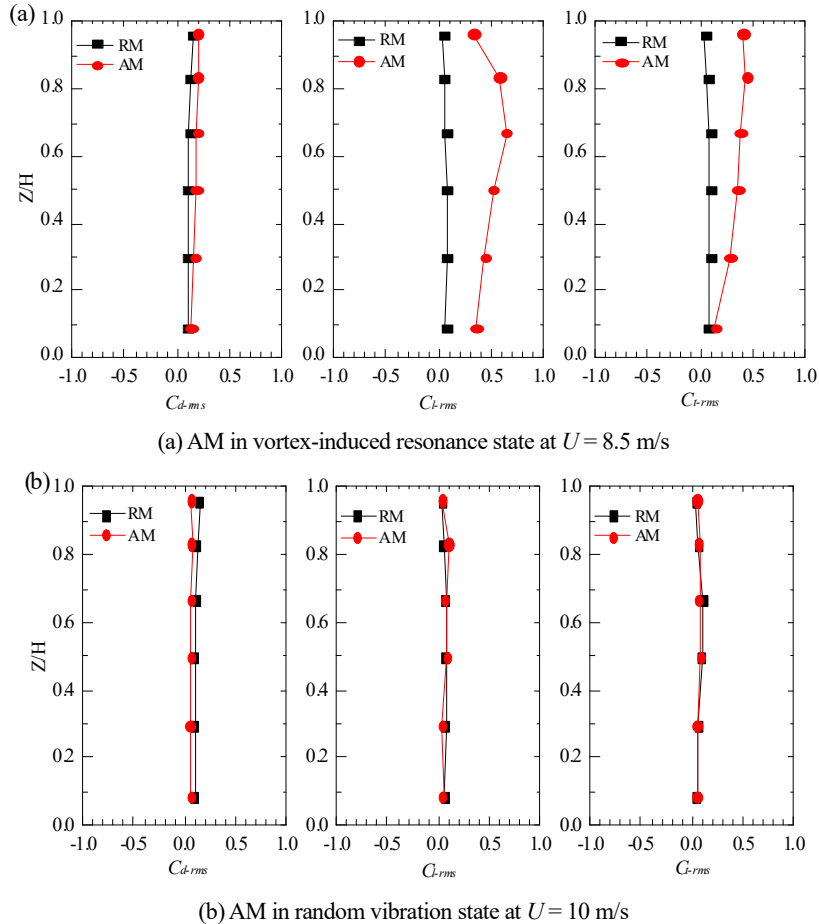

(a) AM in vortex-induced resonance state at $U = 8.5$ m/s

(b) AM in random vibration state at $U = 10$ m/s

Fig. 22 Comparisons of the mean drag force coefficients at each measuring level

(a) AM in vortex-induced resonance state at $U = 8.5$ m/s

(b) AM in random vibration state at $U = 10$ m/s

Fig. 23 Comparisons of the RMS drag force, lift force, and torsional moment coefficients at each measuring level

(a) Across-wind force
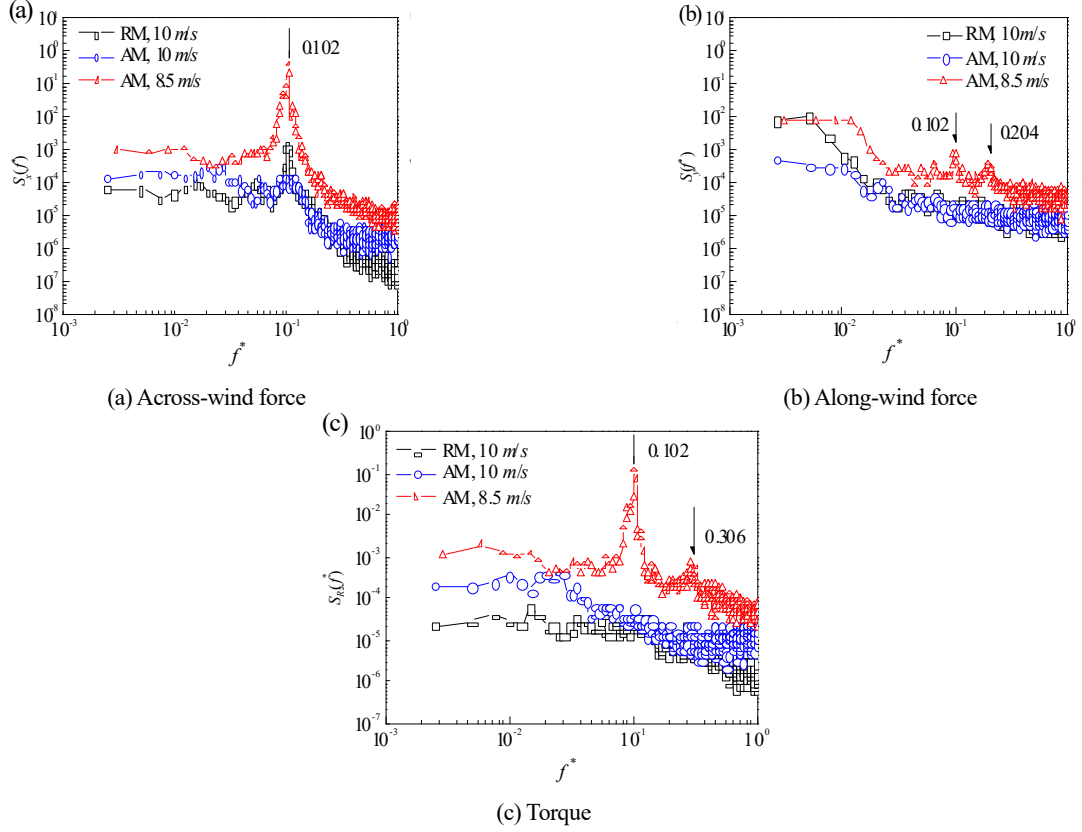
(b) Along-wind force

(c) Torque

Fig. 24 Comparisons of overall aerodynamic spectra between RM and AM

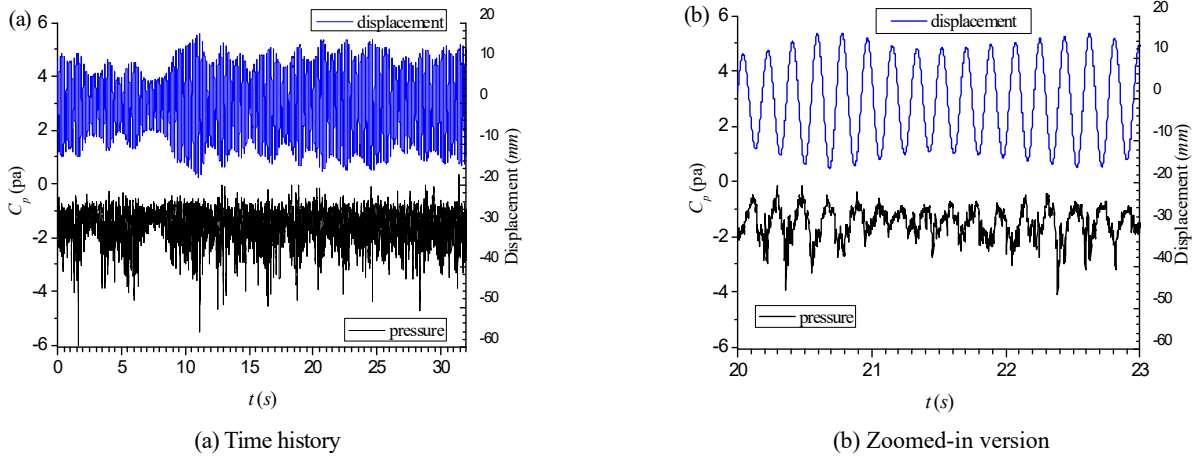(a) Time history

(b) Zoomed-in version

Fig. 25 The pressure signal of tap 4-16 and across-wind top displacement at lock-in

4.2 Aerodynamic feedback effects on aerodynamic forces

Fig. 22 shows the comparisons of the mean drag force coefficients (at each measuring level) between the RM (at the wind speeds of 10 m/s) and the AM at the wind speeds of 8.5 m/s and 10 m/s, corresponding to the vortex-induced resonance and random vibration states, respectively. While the mean drag force coefficients of the AM in the random vibration state at U = 10 m/s are generally slightly larger than those of the RM, their values of AM in the vortex-induced resonance state are significantly larger than those of the RM.

Fig. 23 presents the comparisons of the RMS drag force, lift force, and torsional moment coefficients (at each measuring level) between the RM (at the wind speeds of 10 m/s) and AM at the wind speeds of 8.5 m/s and 10 m/s, corresponding to the vortex-induced resonance and random vibration states, respectively. It can be seen in the figure the RMS drag force, lift force, and torsional moment coefficients of the AM and of the RM are similar to each other when there is no vortex-induced resonance (U = 10 m/s). When vortex-induced resonance occurs, the RMS drag force coefficients of the AM are slightly larger those of the RM, while the RMS lift force and torsional moment coefficients are significantly increased

due mainly to the contribution of the aerodynamic feedback effects.

Fig. 24 gives comparisons of aerodynamic spectra of the overall across-wind force, along-wind force and torque between the RM at wind speed of 10 m/s and AM at wind speeds of 10 m/s and 8.5 m/s. The figure shows that all the aerodynamic spectra of the across-wind force, along-wind force and torque for the AM subjected to vortex-induced resonance are greatly larger than those for the stationary model of RM and those for the vibrating model of AM in the non-lock-in state.

When the AM produces vibrations in the non-lock-in region, the peak value of the across-wind aerodynamic spectrum at the vortex shedding frequency obviously decreases compared to that of RM, indicating that the irregular vibration of the model can actually weaken the vortex shedding. However, the aerodynamic spectra of the across-wind force and torque in the other frequency ranges increase compared to those of the stationary model, while the aerodynamic spectra of the along-wind force decrease at relatively low frequency range.

5. Relationship between vortex shedding and structural displacement at lock-in

Fig. 25 presents the time histories of the pressure signal of tap 4-16 and across-wind top displacement response at the vortex-induced resonance wind speed (8.5 m/s). The figure shows that there is a strong correlation between the displacement and wind pressure on the lateral side. The signals in Fig. 25 include different frequency components, especially for the pressure. To investigate the aerodynamic feedback effects on the vortex shedding in more detail, the signals should be further examined. Hence, the wavelet transform (WT) was used to process the pressure signal of tap 4-16 and the across-wind top displacement response at the vortex-induced resonance wind speed of 8.5 m/s. The WT is an ideal tool for time–frequency analysis and can be regarded as a bandpass filter at various scales. Fig. 26 shows the time–frequency 3D meshing graphs of the processed results. It is observed that the energies are mainly concentrated near the frequency range of approximately [5, 7] Hz; however, the pressure signal includes more high-frequency components.
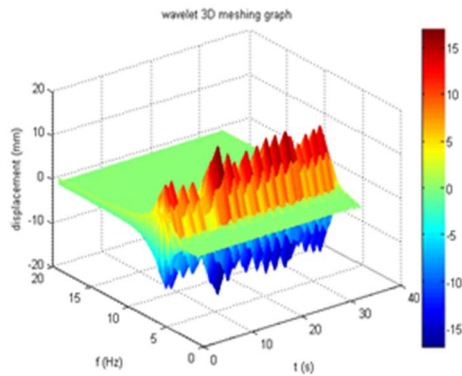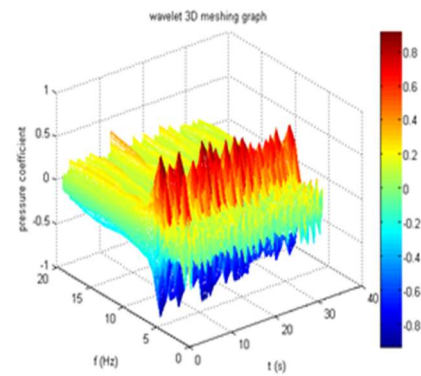
The time histories of the pressure signal of tap 4-16 and the across-wind top displacement response contributed near the 1st across-wind frequency (5.35 Hz) in the vortex-induced resonance state were accordingly extracted, as shown in Fig. 27(a). Although the "simultaneous acquisition" of the scanning valve and laser displacement meter systems has been greatly improved based on the developed in-house data acquisition system, the synchronization of the acquisition still has a certain error due to the different delays of the two acquisition systems. Therefore, a "corrector" should be used to correct the signals in Fig. 27(a). In this study, it has been demonstrated that the delay difference between these two systems is approximately 0.35 s.

The signals after the delay correction are shown in Fig. 27(b). It can be seen that both the amplitudes of wind pressure and displacement response present "beat phenomenon". When the model is at the positive peak displacement, the pressure on measuring point 4-16 is close to the negative peak in a vibration period. Conversely, the pressure on point 4-16 is close to the positive peak in a vibration period when the displacement is at the negative peak. The large amplitude of the displacement envelope corresponds to the large amplitude of the wind pressure envelope that caused by the vortex shedding, and the time delay between these two wave curves is less than ¼ of a vibration period.

Fig. 28 shows the coherence function and phase angle of the pressure signal of tap 4-16 and across-wind top displacement response in the vortex-induced resonance state. As shown in the figure, the value of coherence function is close to 1 (0.98) and the phase angle is around 112.4° near the frequency of vortex shedding (reduced frequency of 0.103), indicating a high correlation is observed between the vortex shedding and across-wind displacement response and the vortex shedding lags behind the across-wind displacement response around 67.6° (1/6~1/4 of a vibration period).

6. Conclusions

To examine the motion-induced aeroelastic (aerodynamic feedback) contributions to the wind-induced effects on a square cylinder in uniform air flow, a series of wind tunnel tests for measuring pressure on a rigid model (RM) and for simultaneously measuring pressure and vibration on an aeroelastic model (AM) have been systematically conducted.

(a) Across-wind top displacement   (b) Pressure

Fig. 26 Time–frequency 3D meshing graphs at vortex-induced resonance wind speed

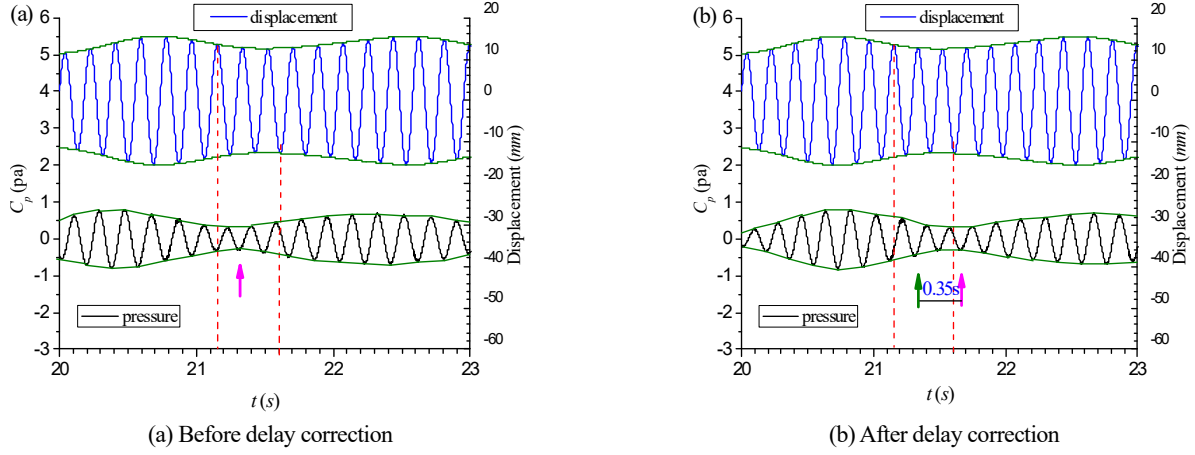(a) Before delay correction

(b) After delay correction

Fig. 27 Time histories of the pressure signal of tap 4-16 and across-wind top displacement response near the 1st across-wind natural frequency at lock-in
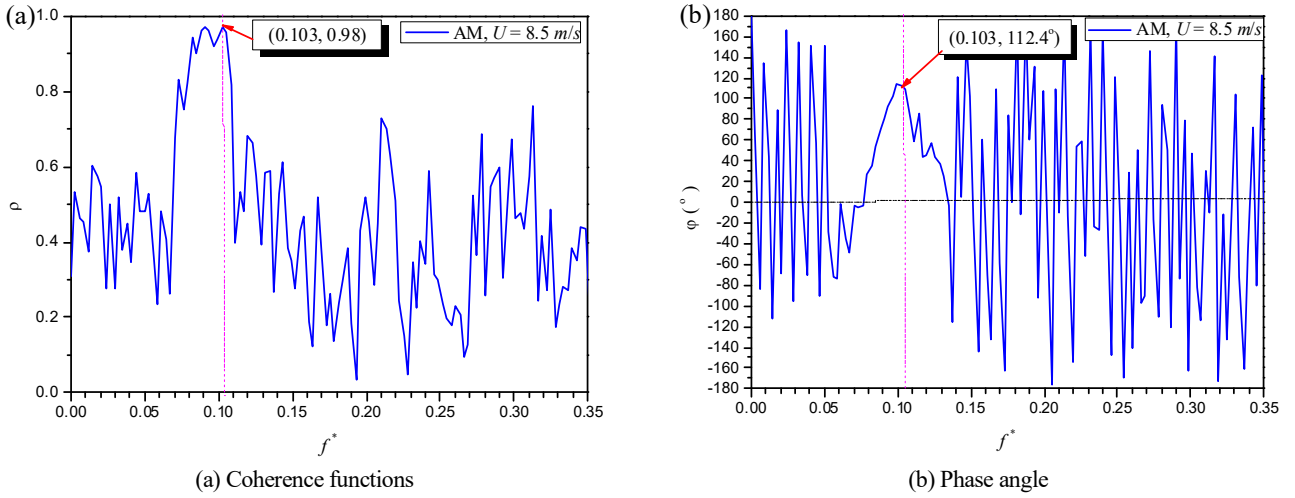

(a) Coherence functions

(b) Phase angle

Fig. 28 Coherence functions and phase angle of the pressure signal of tap 4-16 and across-wind top displacement response at lock-in

The pressures, aerodynamic forces, and structural responses were then obtained with or without considering motion-induced aeroelastic effects. The primary conclusions are as follows:

- The designed AM with simultaneous pressure and vibration measurement, compared to the RM with only pressure measurement, can be used in the wind tunnel tests to conveniently study aeroelastic contributions.
- The aerodynamic feedback effects in the lock-in and non-lock-in regions present obvious difference. While the regularity and energy of vortex shedding could be greatly strengthened in the vortex-excited resonance state, the aerodynamic feedback effects would be weakened in the random vibration state.
- The aerodynamic feedback in the vortex-excited resonance state presents significant unfavorable influences on the mean (mainly on the negative pressure zone) and fluctuating wind pressures, and power spectra and coherence functions (near the across-wind structural natural frequency) of the wind pressures on lateral side. However, the aerodynamic feedback

effects in the random vibration state would increase the absolute values of the mean pressures (mainly on negative pressure zone) but decrease the fluctuating wind pressures, and the power spectra and coherence functions (near the across-wind structural natural frequency) of the wind pressures on lateral side.

- The aerodynamic feedback has remarkable influences on aerodynamic forces (e.g., mean drag force coefficients, fluctuating lift force and torsional moment coefficients) at certain measuring levels in vortex-excited resonance state. However, the aerodynamic feedback effects on aerodynamic forces in random vibration state are generally insignificant.
- In the locked-in region, the aerodynamic feedback effects on the across-wind and torsional fluctuating responses are remarkable, and they are about four times of the results without considering the motion-induced contributions. However, the aerodynamic feedback effects on the wind-induced fluctuating responses in the non-locked-in region are relatively small.
- When the vortex-excited resonance occurs, a high

degree of correlation was observed between the lateral wind pressure and across-wind displacement response (e.g., the frequency and amplitude) with opposite phases.

Acknowledgments

References

Bearman, P.W. (1984), Vortex shedding from oscillating bluff bodies, *Annu. Rev. Fluid Mech*., **16**, 195-222.

Belloli, M., Fossati, F., Giappino, S. and Muggiasca, S. (2014), "Vortex induced vibrations of a bridge deck: Dynamic response and surface pressure distribution", *J., Wind Eng.,* **133**, 160-168. https://doi.org/10.1016/j.jweia.2014.06.005.

Belloli, M., Fossati, F., Giappino, S., Muggiasca, S. and Villani, M. (2011), "On the aerodynamic and aeroelastic response of a bridge tower", *J. Wind Eng*., **99**(6-7), 729-733. https://doi.org/10.1016/j.jweia.2011.03.013.

Blevins, R.D. (1990), *Flow-Induced Vibration, 2nd edition Van Nostrand Reinhold*, New York, NY, USA.

Chen, W.L. and Xu, F. (2012), "Investigation of a hybrid approach combining experimental tests and numerical simulations to study vortex-induced vibration in a circular cylinder", *J. Sound Vib*., **331**(5), 1164-1182. https://doi.org/10.1016/j.jsv.2011.10.016.

Dongmei, H., Xue, Z., Shiqing, H., Xuhui, H. and Hua, H. (2017b), "Characteristics of the aerodynamic interference between two high-rise buildings of different height and identical square cross-section", *Wind Struct., Int. J.*, **24**(5), 501-528. https://doi.org/10.12989/was.2017.24.5.501.

Dyrbye, C. and Hansen, S.O. (1996), *Wind Loads on Structures*, John Wiley & Sons, Chichester, England.

Ehrmann, R.S., Loftin, K.M., Johnson, S. and White, E.B. (2014), "Lock-in of elastically mounted airfoils at a 90° angle of attack", *J. Fluid. Struct*., **44**, 205-215. https://doi.org/10.1016/j.jfluidstructs.2013.10.008.

Ehsan, F. and Scanlan, R.H. (1990), "Vortex-induced vibrations of flexible bridges", *J. Eng. Mech.-ASCE*, **116**(6), 1392-1411.

Gu, M. and Quan, Y. (2004), "Across-wind loads of typical tall buildings", *J. Wind Eng*., **92**(13), 1147-1165. https://doi.org/10.1016/j.jweia.2004.06.004.

Holmes, J.D. and Lewis, R.E. (1987), Optimization of dynamics-pressure-measurement systems I. & II, *J. Wind Eng*., **25**, 249-290. https://doi.org/10.1061/(ASCE)0733-9399(1990)116:6(1392)

Huang, D.M. and He, S.Q. (2016), Synchronous pressure and vibration measurement system and implementation method based on aeroelastic model., patent, CN201610176152.6. [In Chinese]

Huang, D.M., He, S,Q., He, X.H. and Zhu, X. (2017c), "Prediction of wind loads on high-rise building using a BP neural network combined with POD", *J. Wind Eng*., **170**, 1-17.

https://doi.org/10.1016/j.jweia.2017.07.021.

Huang, D.M., Zhu, L.D, Ding, Q.S., Zhu, X. and Chen, W. (2017a), "Aeroelastic and aerodynamic interference effects on a high-rise building", *J. Fluid. Struct*., **69**, 355-381. https://doi.org/10.1016/j.jfluidstructs.2017.01.007.

Huang, D.M., Zhu, L.D. and Chen, W. (2014), "Power spectra of wind forces on a high-rise building with section varying along height", *Wind Struct*., *Int. J*., **18**(3), 295-320. https://doi.org/10.12989/was.2014.18.3.295.

Huang, D.M., Zhu, L.D. and Chen, W. (2015a), "Vertical coherence functions of wind forces and influences on wind-induced responses of a high-rise building with section varying along height", *Wind Struct., Int. J.,* **21**(2), 119-158. https://doi.org/10.12989/was.2015.21.2.119.

Huang, D.M., Zhu, L.D. and Chen, W. (2015b), "Covariance proper transformation-based pseudo excitation algorithm and simplified SRSS method for the response of high-rise building subject to wind-induced multi-excitation", *Eng. Struct.*, **100**(1), 425-441. https://doi.org/10.1016/j.engstruct.2015.05.040.

Huang, D.M., Zhu, L.D., Ren, W.X. and Ding, Q.S. (2018), "A harmonic piecewise linearization-wavelet transforms method for identification of non-linear vibration "black box" systems: application in wind-induced vibration of a high-rise building", *J. Fluid. Struct*., **78**, .239-262. https://doi.org/10.1016/j.jfluidstructs.2017.12.021.

Katagiri, J., Ohkuma, T. and Marikawa, H. (2001), "Motion-induced wind forces acting on rectangular high-rise buildings with side ratio of 2", *J. Wind Eng*., **89**(14-15), 1421-1432. https://doi.org/10.1016/S0167-6105(01)00148-9.

Kikitsu, H., Okuda, Y., Ohashi, M. and Kand, J. (2008), "POD analysis of wind velocity field in the wake region behind vibrating three-dimensional square prism", *J. Wind Eng. Ind. Aerod*., **96**, 2093-2103.

Mannini, C., Marra, A.M. and Bartoli, G. (2014), "VIV–galloping instability of rectangular cylinders: Review and new experiments", *J. Wind Eng. Ind. Aerod*., **132**, 109-124.

Marra, A.M., Mannini, C. and Bartoli, G. (2011), "Van der Pol-type equation for modeling vortex-induced oscillations of bridgedecks", *J. Wind Eng*., **99**(6-7), 776-785. https://doi.org/10.1016/j.jweia.2011.03.014.

Sarpkaya, T. (1979), Vortex-induced oscillations: a selective review, *J. Appl. Mech*., **46**(2), 241-258.

Simiu, E. and Scanlan, H. (1996), *Wind Effects on Structures*, Wiley, New York, NY, USA.

Williamson, C.H.K. (1996), "Vortex dynamics in the cylinder wake", *Annu. Rev. Fluid Mech.*, **28**, 477-539. https://doi.org/10.1146/annurev.fl.28.010196.002401.

Williamson, C.H.K. and Govardhan, R. (2008), "A brief review of recent results in vortex-induced vibrations", *J. Wind Eng*., **96**, 713-735. https://doi.org/10.1016/j.jweia.2007.06.019.

Wu, T. and Kareem, A. (2012), "An Overview of Vortex-Induced Vibration (VIV) of Bridge Decks", *Frontiers of Structural and Civ. Eng*., **6**(4), 335-347.

Wu, T. and Kareem, A. (2013), "Vortex-induced vibration of bridge decks: Volterra series-based model", *ASCE J. Eng. Mech.*, **139**(12), 1831-1843. https://doi.org/10.1061/(ASCE)EM.1943-7889.0000628.

Wu, T. and Kareem, A. (2015), "A low-dimensional model for nonlinear bluff-body aerodynamics: A peeling-an-onion analogy", *J. Wind Eng*., **146**, 128-138. https://doi.org/10.1016/j.jweia.2015.08.009.

Yen, S.C. and Hsu, C.M. (2007), "Flow patterns and wake structure of a swept-back wing", *AIAA J.*, **45**, 228-236. https://doi.org/10.2514/1.24045.

Yen, S.C. and Yang, C.W. (2011), "Flow patterns and vortex shedding behavior behind a square cylinder", *J. Wind Eng*., **99**(8), 868-878. https://doi.org/10.1016/j.jweia.2011.06.006.

Zasso, A., Belloli, M., Giappino, S. and Muggiasca, S. (2008), "Pressure field analysis on oscillating circular cylinder", *J. Fluid. Struct.*, **24**, 628-650.
https://doi.org/10.1016/j.fluidstructs.2007.11.007.

Zheng, C., Liu, Z., Wu, T., Wang, H., Wu, Y. and Shi, X. (2019), "Experimental investigation of vortex-induced vibration of a thousand-meter-scale mega-tall building", *J. Flui. Struct.*, **85**, 94-109.
https://doi.org/10.1016/j.fluidstructs.2018.12.005.

Zhu, L.D., Meng, X.L. and Guo, Z.S. (2013), "Nonlinear mathematical model of vortex-induced vertical force on a flat closed-box bridge deck", *J. Wind Eng.*, **122**, 69-82.
https://doi.org/10.1016/j.jweia.2013.07.008.

AD